Available online at www.sciencedirect.com

ScienceDirect

Acta Materialia 68 (2014) 42–51

Acta MATERIALIA

www.elsevier.com/locate/actamat

Influence of Fe-rich intermetallics on solidification defects in Al–Si–Cu alloys

C. Puncreobutr [a,b], P.D. Lee [b,*], K.M. Kareh [a], T. Connolley [c], J.L. Fife [d], A.B. Phillion [e]

[a] Department of Materials, Imperial College London, Prince Consort Road, London, UK
[b] School of Materials, The University of Manchester, Oxford Road, Manchester, UK
[c] Diamond Light Source Ltd., Harwell Science & Innovation Campus, Didcot, UK
[d] Swiss Light Source, Paul Scherrer Institut, 5232 Villigen PSI, Switzerland
[e] School of Engineering, The University of British Columbia, Kelowna, Canada

Received 27 October 2013; received in revised form 9 December 2013; accepted 3 January 2014
Available online 12 February 2014

Abstract

To better understand the influence of Fe-rich intermetallics on solidification defect formation, fast in situ synchrotron X-ray tomographic microscopy experiments were performed on a commercial A319 alloy (Al–7.5Si–3.5Cu, wt.%) with 0.2 and 0.6 wt.% Fe. Real-time observations during solidification and semi-solid deformation experiments reveal that β-intermetallics contribute via several different mechanisms to porosity formation and hot tearing susceptibility. While β-intermetallics were not observed to nucleate porosity directly, they do block interdendritic channels, thereby reducing the shrinkage feeding, and increasing pore tortuosity. Pores also grow preferentially along the surface of the β-intermetallics, suggesting that the β-phase has a lower gas–solid interfacial energy than α-Al, thus assisting in increasing pore volume. During uniaxial tension experiments, the ductile failure of the semi-solid, intermetallic-poor, base alloy transitions to a brittle-like failure when a large amount of β-intermetallics are present. In all post-failure microstructures, internal damage was preferentially orientated perpendicular to the loading direction, agreeing with prior experimental and numerical studies.

Keywords: Intermetallics; Al–Si–Cu alloys; Porosity; Hot tearing; X-ray tomographic microscopy

1. Introduction

The excellent mechanical properties of Al–Si–Cu casting alloys have enabled this alloy family to find usage in many automotive applications, such as engine blocks and cylinder heads [1]. However, using recycled-grade Al–Si–Cu alloys as the base material for structural components remains a major challenge, especially when fatigue life is critical [2], because iron is easily picked up during the recycling process. The increased Fe content can be sufficient to promote the formation of coarse Fe-rich intermetallic compounds, including plate-like β-Al_5FeSi intermetallics, which have been shown to act as crack initiators and are thus detrimental to in-service mechanical properties [2–6]. In addition to their negative effects on the mechanical properties of the final product, β-Al_5FeSi intermetallics are also reported to be deleterious to castability, increasing the as-cast porosity content [7–10]. Many mechanisms by which β-Al_5FeSi intermetallics affect pore formation have been suggested, including blocking of interdendritic flow [10,11], acting as nucleation sites [12] and aiding pore growth [13]. They may also influence pore growth indirectly, e.g. inducing larger Al–Si eutectic grains that reduce feeding and thus increase porosity [14]. However, there has been no consensus on the choice of a

* Corresponding author.
E-mail address: peter.lee@manchester.ac.uk (P.D. Lee).

http://dx.doi.org/10.1016/j.actamat.2014.01.007

dominant mechanism due to most studies providing only post-mortem analyses.

One important Al–Si–Cu casting alloy is A319, which exhibits a propensity to form plate-like β-Al_5FeSi intermetallics. In addition to as-cast porosity, A319 alloy castings are susceptible to hot tearing [15,16], another solidification defect that limits production yield during the casting of recycled aluminium. The formation of hot tears is a complex phenomenon caused by insufficient liquid feeding compensating for solidification shrinkage in the presence of thermal stresses and strains [17]. While an extensive number of experimental and numerical investigations have been conducted on binary alloys to relate various alloying and processing parameters to hot-tearing susceptibility [17–20], little is known about hot tearing in commercial Al–Si–Cu casting alloys, and even less about the influence of β-intermetallics. At the scale of the process, it has been shown that the addition of Sr and/or TiB_2 can have a beneficial effect in reducing the hot-tearing susceptibility of A319 alloys [15,16]. In parallel, Sr modifications [9] and TiB_2 grain-refiner additions [21] have been found to greatly alter microstructure, i.e. the size and morphology of plate-like β-intermetallics. However, the role of β-intermetallics on hot-tear formation has not been directly examined, and the correlation between elements that modify microstructure and reduction in hot tearing is still unclear.

Direct observation of defect formation during solidification has recently been made possible both in two dimensions, via X-ray radiography, and in three dimensions, via X-ray tomographic microscopy, yielding better insights into real-time pore formation [22–25] and hot-tearing processes [26–30] in binary Al–Cu alloys. Over the past two decades real-time observation has also enabled quantitative studies of microstructure evolution and secondary phase formation during solidification [31–33] and coarsening [34,35], as reviewed by Maire and Withers [36]. In the present study, fast in situ synchrotron X-ray tomographic microscopy experiments were performed on commercial A319 alloys (Al–7.5Si–3.5Cu, wt.%) with differing Fe-levels (0.2–0.6 wt.% Fe). Real-time 3-D observations of porosity and hot-tear formation were made during both in situ solidification and semi-solid uniaxial tension experiments to provide a greater understanding of the influence of β-intermetallics on defect formation in the semi-solid state.

2. Experimental methodology

2.1. Materials

To perform the solidification and semi-solid deformation experiments, A319 alloys (Al–7.5Si–3.5Cu, wt.%) with two different levels of Fe (0.2–0.6Fe, wt.%) were prepared from a commercial A319 ingot (as-received from Ford Motor Company) and a commercially pure Al–10Fe (wt.%) master alloy. These metals were melted using an electric-resistance furnace in a clay-bonded graphite crucible at 730 °C and were then cast into a pre-heated well-fed permanent mould [37] to form a wedge-shaped specimen. The resulting microstructure was equiaxed with an as-cast secondary dendrite arm spacing of ~30 μm. The chemical compositions obtained using X-ray fluorescence were found to be Al–7.49Si–3.4Cu–0.15Fe (wt.%) and Al–7.52Si–3.53Cu–0.59Fe (wt.%) for alloys with 0.2 wt.% Fe and 0.6 wt.% Fe, respectively.

The fraction of intermetallics, f_I, for these two alloy compositions is plotted in Fig. 1 using a Scheil approximation within the Thermo-Calc software (Thermo-Calc, Sweden) and the database from Ref. [38]. The thermodynamic calculation predicts a 3-fold increase in β-intermetallic phase fraction, from ~0.65% to nearly 2.1% as the Fe content is increased from 0.2 to 0.6 wt.%. Longitudinal sections of the as-cast microstructure from the high-resolution tomography images (0.9 μm), described in Section 2.3, for both wedge castings are also shown in Fig. 1. Fig. 1 shows that the plate-like β-intermetallics can only be resolved in the specimen with 0.6 wt.% Fe. The β-intermetallic phase cannot be resolved with the given spatial resolution in the specimen with 0.2 wt.% Fe and cooled at the rates given by the wedge casting setup. Thus, the 0.2 wt.% Fe alloy corresponds to a primary-grade material while the 0.6 wt.% Fe alloy corresponds to a recycled-grade product.

Subsequent to the wedge-casting, a tensile specimen was extracted from the 0.2 wt.% Fe wedge for the in situ

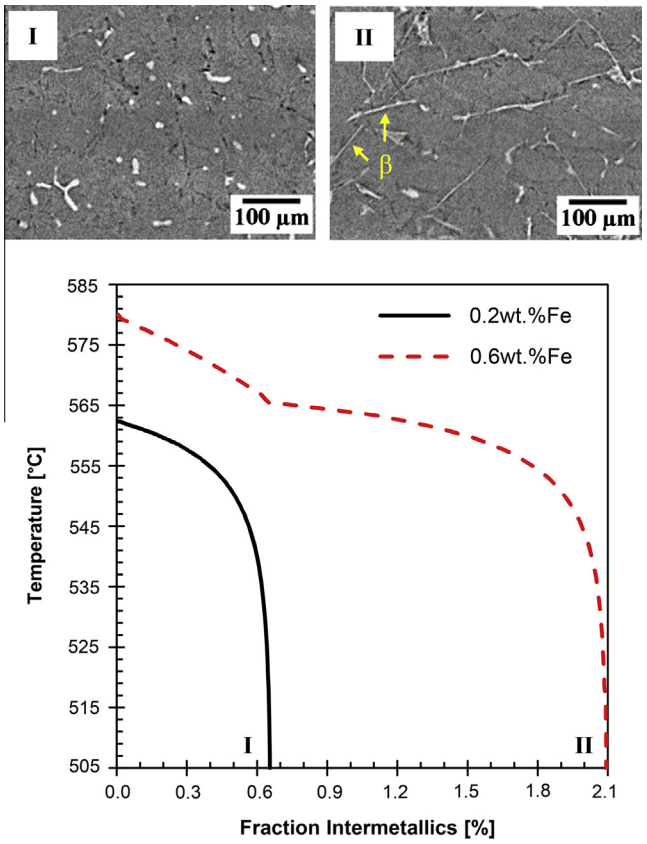

Fig. 1. Calculated fraction of the β-intermetallics in Al-A319 alloys at two Fe levels of (I) 0.2 wt.% Fe and (II) 0.6 wt.% Fe, assuming the Scheil solidification model. (I) and (II) show high-resolution longitudinal sections of typical as-cast solidified microstructures.

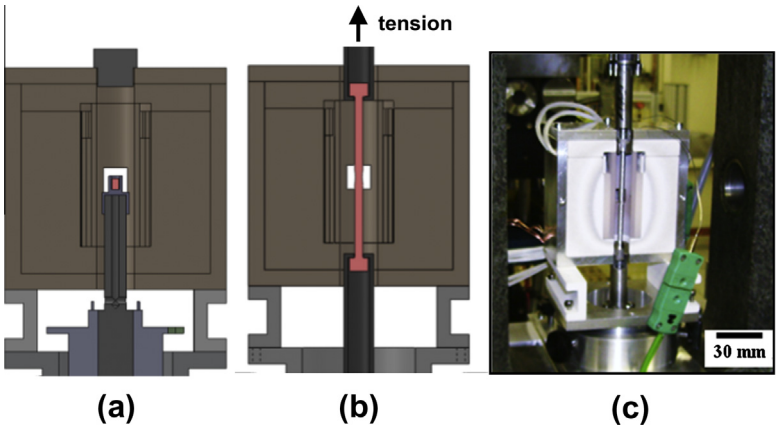

Fig. 2. (a and b) Schematics of experimental setups for solidification and semi-solid uniaxial tension studies, respectively. (c) Photograph of the thermomechanical testing rig with the furnace in place.

semi-solid deformation experiment, and both a cylindrical specimen and a tensile specimen were machined from the 0.6 wt.% Fe wedge for the in situ solidification and semi-solid deformation experiments. The dimensions of the tensile specimens were 3 mm in diameter and 60 mm in length, both with a small central gauge notched section of 2.5 mm in diameter and 5.5 mm in length. The cylindrical specimen was 2.5 mm in diameter and 4 mm in length.

2.2. Solidification experiment

To investigate the interaction between β-intermetallics and porosity formation, one in situ solidification experiment was performed at the TOMCAT beamline of the Swiss Light Source (SLS, Paul Scherrer Institut, Switzerland) using a bespoke resistance furnace (shown in Fig. 2a). A further description of the setup on the TOMCAT beamline can be found in Refs. [39–41] and of the bespoke furnace in Ref. [42]. In this test, the 0.6 wt.% Fe specimen was heated to 650 °C (as measured by a K-type thermocouple located underneath the specimen holder) and held for 5 min to ensure it was completely molten. The specimen was then cooled at a rate of 0.05 °C s^{-1} until completely solid. During solidification, the specimen was continuously rotated and polychromatic X-rays[1] were used to acquire a series of 2-D radiographic projections at different angles. The projections were then processed to reconstruct 3-D tomographic volumes with a pixel size of 2.75 μm. Each complete 3-D volume consisted of 1001 projections captured in a total time of 2 s, minimizing the dynamic change in the solidifying microstructure during each scan. There was a delay of 70 s to download the images from the camera memory, resulting in a total scan time of 72 s between consecutive 3-D volumes.

[1] Polychromatic X-rays filtered to 5% power (an average energy of ~30 keV) were used in this work to achieve the high flux needed to acquire a complete 3-D volume in 2 s.

2.3. Semi-solid deformation experiment

To study the behaviour of semi-solid A319 alloys during tensile deformation, the resistance furnace used for the solidification experiment was integrated with a bespoke mechanical tester rig, called the P2R, shown in Fig. 2b and c. Full details about this apparatus can be found in Ref. [27]. The two in situ tensile deformation experiments were then performed on the 0.2 and 0.6 wt.% Fe specimens at the I12 beamline of the Diamond Light Source (Harwell Science and Innovation Campus, UK). In these tests, each specimen was heated to 515 °C and held for 5 min to achieve thermal equilibrium. This temperature is just above the eutectic temperature (510 °C [31]) and corresponds to a solid fraction (f_s) of > 0.9 in the notched region. Then, each specimen was deformed until failure under uniaxial tension at a constant crosshead displacement rate of 10 μm s^{-1}, corresponding to an average axial strain rate of $\sim 5 \times 10^{-3}$ s^{-1}. During deformation, the specimen was continuously rotated and a monochromatic X-ray energy of 53 keV was used to acquire a series of 2-D radiographic projections at different angles. The projections were then processed to reconstruct a series of 3-D tomographic volumes with a pixel size of 12.22 μm. Each 3-D volume was captured using 720 projections in a total time of 4 s. 24 volumes were acquired for each deformation test specimen from the undeformed to the final failure stages with a 4 s downtime between consecutive 3-D volumes. After final failure, a high-resolution synchrotron X-ray tomographic microscopy scan with a pixel size of 0.9 μm was performed on the upper half of each failed specimen (which was clamped in the moving jaw (Fig. 2b)) to further investigate the fracture surface in three dimensions.

2.4. Quantitative characterization

A fast reconstruction algorithm based on the Fourier transform method (gridrec) [43,44] was used to obtain the 3-D solidification datasets, while an algorithm based on

the filtered back projection (FBP) method [45–47] was used to obtain the 3-D semi-solid deformation datasets. Different algorithms were used as each beamline has its own process for reconstructing the tomographic images. Although significant differences in computational performance can be found, the reconstructed 3-D results obtained from gridrec and FBP are almost equivalent [43]. In both cases, a flat-field correction, a dark-field correction and ring-artefact removal algorithm [45,48] were performed prior to reconstruction. For each experiment, the series of 3-D volumes was then spatially aligned using a 3-D affine registration method [49], and then a 3-D non-linear diffusion filter [50] was applied to reduce noise. Finally, region growing segmentation [51] was used to obtain pores and hot tears whereas manual segmentation was performed to obtain the β-intermetallic phase.

For the solidification experiment, the quantification of pore and intermetallic phases was made in a sub-volume of $400 \times 400 \times 400$ voxels^3 (equivalent to $\sim$1 mm^3) extracted from a region near the specimen surface to focus on the evolution of a single pore and its interaction with the surrounding β-intermetallics. For the semi-solid deformation experiments, the quantification was made in the gauge region of the specimens. The volume analyzed in the gauge was kept constant and hence was elongated proportional to the strain undertaken by the specimen from the undeformed state to failure. Note that in this paper the term "pores" is used when the region is formed due to solidification shrinkage/feeding, the term "voids" is used when the region is formed during straining, and "damage" is used for the combination of the two regions. Two types of pores/voids were defined in the gauge: internal (if the pore/void had no connectivity to the specimen surface) and surface-connected (if the pore connected to the surface). The volume and orientation of each pore/void and each intermetallic was calculated using a marching-cube triangulation method and principle component analysis (PCA), respectively [52,53]. These calculations were performed using MATLAB (MathWorks, MA). An advanced rendering package (Avizo, VSG, France) was used to produce the visualizations of all 3-D structures.

3. Results and discussion

3.1. Effect of intermetallics on porosity formation during solidification

The evolution of a selected (typical) pore in the Al–Si–Cu alloy with 0.6 wt.% Fe during the solidification experiment is examined in Fig. 3. The 3-D rendering of the pore with decreasing temperature is shown in Fig. 3a, and the corresponding evolution in pore volume and sphericity is quantified in Fig. 3b. The pore first appears at 565 ± 1 °C, and is small and round (Fig. 3a-I). As the temperature decreases to 561 ± 1 °C (Fig. 3a-II), the pore grows very rapidly, tripling its initial volume of 5×10^3 mm^3 (black dots in Fig. 3b). This trend continues

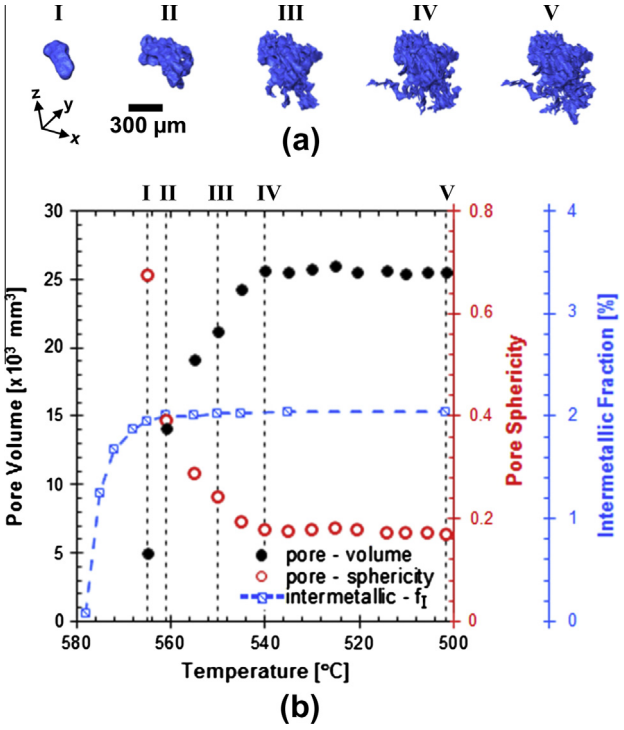

Fig. 3. (a) 3-D evolution of a pore during solidification (I–V represent temperatures of 565, 561, 550, 540 and 502 °C, respectively). (b) Quantified volume (black dots) and sphericity (red circles) of the pore shown in (a). The quantified fraction of intermetallics is also illustrated in blue. (For interpretation of the references to colour in this figure legend, the reader is referred to the web version of this article.)

with subsequent solidification (Fig. 3a-III, IV), where both pore size and tortuosity increase. Pore formation is almost complete at 540 ± 1 °C when the pore reaches a volume of $\sim 26 \times 10^3$ mm^3 (Fig. 3a-V). At lower temperatures, the pore volume remains constant, as shown by the plateau of black dots in Fig. 3b. The quantified sphericity of the pore, which is a measure of its roundness (where the sphericity of a sphere equals 1), decreases dramatically from $\sim$0.7 when it first forms to <0.2 after 540 ± 1 °C, and remains unchanged thereafter (red circles in Fig. 3b).

The observed evolution in β-intermetallics is also plotted in Fig. 3b (blue curve) for comparison purposes. β-intermetallics are observed to form between 578 ± 1 and 565 ± 1 °C, i.e. their formation is mostly complete when the observed pore nucleates at 565 ± 1 °C. Plate-like β-intermetallics are thus already present at the moment of pore nucleation. Note that the observed nucleation temperature of β-intermetallics is in good agreement with prior in situ solidification studies [31,54].

To clarify the role of β-intermetallics on pore nucleation and growth, the interaction between the selected pore and its surrounding intermetallics during solidification is rendered in three dimensions in Fig. 4. The pore (blue) first forms inside a liquid channel that is surrounded by β-intermetallics (red). These intermetallics have been reported to block interdendritic flow, reducing permeability [55]. It has also been hypothesized that they block

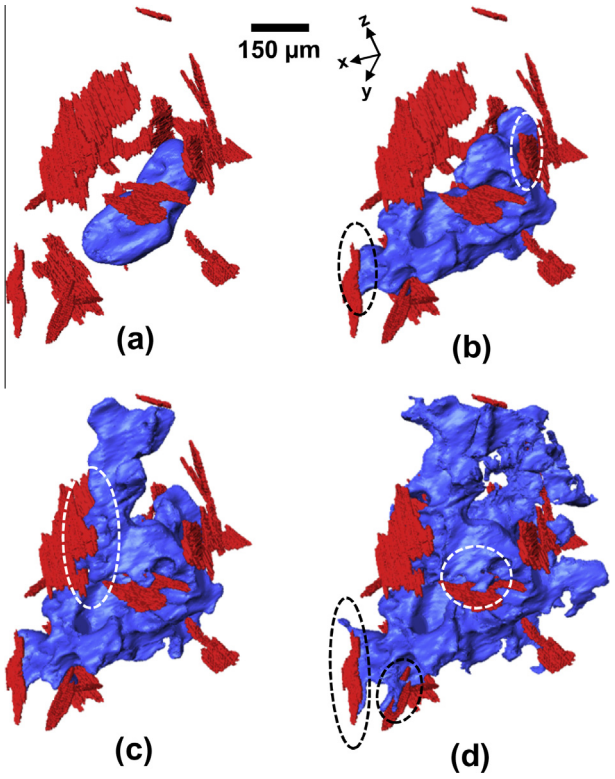

Fig. 4. 3-D rendering of pore evolution (blue) in the presence of intermetallics (red) at: (a) 565 °C, (b) 561 °C, (c) 555 °C and (d) 550 °C. Examples of pore growth along the solid surface of intermetallics are shown in dashed black and white circles. (For interpretation of the references to colour in this figure legend, the reader is referred to the web version of this article.)

hydrogen diffusion paths in the interdendritic liquid by acting as diffusion barriers, which imposes hydrogen supersaturation in local, subdivided domains and induces pore nucleation [13]. These hypotheses agree well with Fig. 4, where the liquid channel will be supersaturated with hydrogen and will exhibit a lower permeability due to the number of β-intermetallics surrounding it. After nucleation, the pore grows very rapidly into the interdendritic regions with an increasing tortuosity as shown in Fig. 4b and d. The growth of the pore is physically constrained by both β-intermetallics and other solid phases, i.e. the primary dendrites and the Al–Si eutectic (which starts nucleating at 561 ± 1 °C). Similar behaviour of pore growth constrained by the solid phases was previously observed radiographically [22] and tomographically [56]. The pore also appears to grow preferentially along the solid surfaces of the β-intermetallic plates, wicking along the intermetallic in preference to either growing into the interdendritic liquid or along the α-Al dendrites (shown in the dashed black and white circles in Fig. 4b and c). One hypothesis to explain the accelerated pore growth along the surface of the intermetallics is that the Fe-rich intermetallic–gas interfacial energy could be less than those of the gas–liquid or gas–α-Al interfaces [13]. Although not shown here, similar behaviour was also observed in other pores presented in the specimen, but a statistical analysis was not possible due to the limited number of pores present in the analyzed volume.

Unlike prior work involving quenched microstructure observations (e.g. [12]), there was no evidence of pore nucleation on β-intermetallics in the tomographic images shown in Fig. 4. The results of this in situ solidification experiment instead suggest that β-intermetallics induce pore nucleation by blocking the feeding of liquid, thus reducing permeability and accelerating pore growth along the surfaces of intermetallics. The quantitative characterization is, however, limited to one example under specific cooling conditions, and further investigations are needed to confirm the predominance of this mechanism. The in situ observation of preferential pore growth along the planar surfaces of β-intermetallics shown in Fig. 4d may also explain why other authors have frequently found pores in contact with β-intermetallics in classical quenched microstructures (e.g. [9,12,57]); pores appear to nucleate in the interdendritic liquid and/or off the aluminium dendrites and then later grow towards and make contact with surrounding intermetallics.

3.2. Effect of intermetallics on hot-tear formation

3.2.1. In situ observation

The longitudinal sections in Fig. 5 show the evolution of damage with increasing strain for both 0.2 and 0.6 wt.% Fe Al–Si–Cu specimens in semi-solid uniaxial tension. Fig 5a–d (e–h) shows the evolving structure of the 0.2 wt.% Fe (0.6 wt.% Fe) specimen undergoing 0–19% (0–7%) strain. The images show that the attenuation contrast is sufficient for the quantification of damage formation in the complex dendritic microstructure—where the damage appears as dark regions, equiaxed aluminium grains appear as grey regions, and the liquid and intermetallic phases (including β-Al_5FeSi and Al_2Cu) appear as white regions. Although the pixel size of 12.22 μm used in this in situ study is sufficient to quantify damage formation over the entire specimen gauge length, the β-intermetallics are too fine for quantitative analysis. By segmenting the pores, voids and developing damage, the in situ damage evolution during hot tearing can be rendered as shown in Fig. 6a and b. The true strains in all 3-D renderings are identical to those shown in the longitudinal sections of Fig. 5, and the internal and surface-connected damage are shown in blue and red, respectively. The corresponding development of the volume of total damage is quantified and plotted in Fig. 6c.

Before deformation is applied, it is observed that only small as-cast pores are present in the semi-solid microstructure of both specimens (Fig. 6a-I and b-I). Also, as shown in the high-resolution scans of Fig. 1, the specimen at 0.2 wt.% Fe does not appear to contain β-intermetallics, while the specimen at 0.6 wt.% Fe exhibits large plate-like structures. Beginning with the specimen at 0.2 wt.% Fe (Fig. 6a), it can be seen that new voids nucleate in the middle of the specimen gauge only after a large amount of true strain (~14%) has been applied (Fig. 6a-II), and

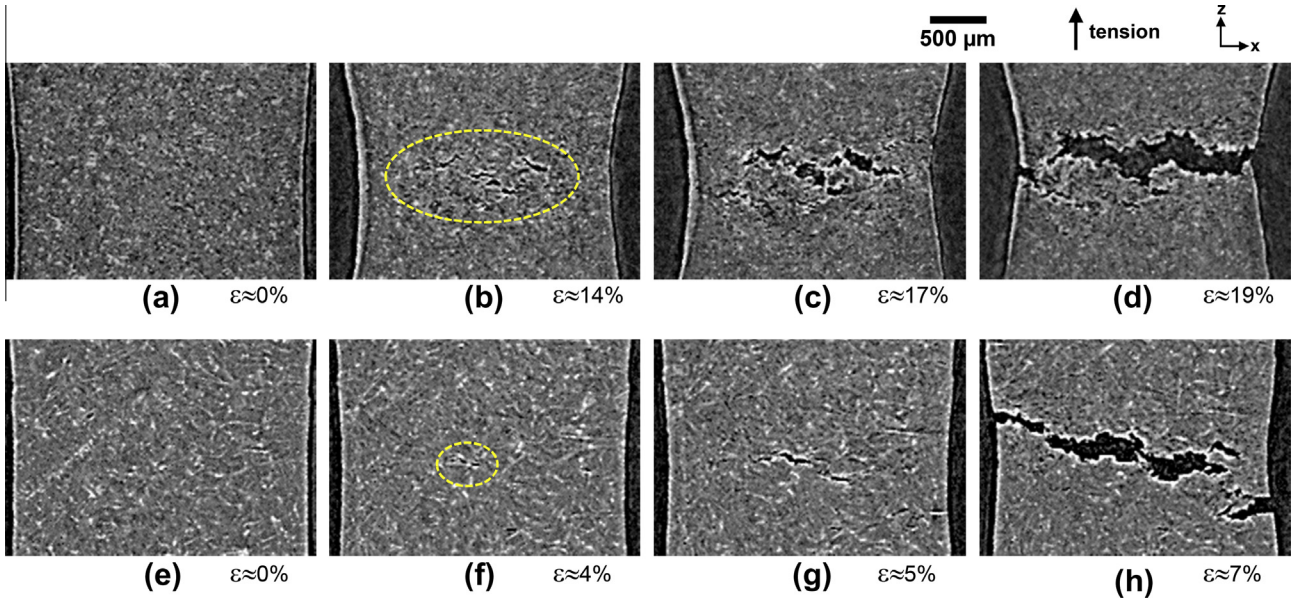

Fig. 5. Typical evolution of damage during simulated hot tearing in Al–7.5Si–3.5Cu with (a–d) 0.2 wt.% Fe and (e–h) 0.6 wt.% Fe. Note that (a–d) represent true strains (%) of 0, 14, 17, 19, respectively, and (e–h) represent true strains (%) of 0, 4, 5, 7, respectively. Dashed yellow circles indicate locations where critical damage initiated. (For interpretation of the references to colour in this figure legend, the reader is referred to the web version of this article.)

there is a steady increase in the internal damage (Fig. 6c). There is also considerable deformation and necking in the gauge region. Note that the true strain was measured by the equation $\varepsilon = \ln(L/L_0)$, where L_0 is the initial length of the analyzed central gauge region (4 mm). A further increase in strain, to a true strain of 17%, leads to additional void nucleation, existing damage growth and the commencement of damage coalescence (Fig. 6a-III). This is characterized by a sharp increase in the internal damage of the specimen (Fig. 6c). Final failure occurs when the majority of internal damage joins and then connects to the specimen surface (Fig. 6a-IV) at a true strain of 19%. This is characterized by a sharp drop in the internal damage volume mirrored by an increase in the total volume of surface-connected damage, both shown in Fig. 6c, and this corresponds to the moment when the interconnected network of internal damage reaches the specimen surface.

In comparison, the 0.6 wt.% Fe specimen displays a much more brittle-like failure mechanism (Fig. 6). Voids form initially near the middle of specimen gauge (Fig. 6b-II) where triaxiality is the greatest [59] (see Supplementary Fig. F1 for triaxiality evolution calculated via a method given in Ref. [58]), but this occurs at a much lower true strain of ~4%, when compared to the 0.2 wt.% Fe specimen (Fig. 6a-II) ($\varepsilon \approx 14\%$). Rapid void growth and coalescence are then observed between true strains of 4% and 5% (qualitatively observed in Fig. 6b-III and quantitatively shown in Fig. 6c), but there is only a limited amount of necking in the gauge region. Final failure occurs at a true strain of ~7% when most of the damage coalesces across the gauge and reaches the specimen surface (Fig. 6b-IV). This moment is quantified in Fig. 6c, where a sharp increase in the total volume of surface-connected damage is observed.

It is known from prior in situ studies with finer resolution but smaller volumes [26,28,29] that semi-solid tensile deformation promotes the flow of liquid metal to strain-localized regions, leading to regional liquid accumulation that can accommodate the applied strains. If liquid feeding is insufficient, strain cannot be accommodated and hot tears may form. In the specimen with 0.2 wt.% Fe, there are small, unresolved intermetallics, and liquid flow occurs with ease and can thus accommodate a large amount of strain ($\varepsilon \approx 14\%$). With increasing strain, the liquid supply becomes insufficient and voids first form internally over a large portion of the core where strain and triaxiality are the greatest [27,59,60]. They then grow outwards toward the surface (Fig. 6a), which occurs through a combination of void nucleation, growth and coalescence. Similar phenomena were previously observed in binary Al–Cu [26,27] and other commercial alloys [61]. Terzi et al. [28], in contrast, qualitatively observed that the damage appears to grow in from the surface of the specimen starting from existing pores located near the specimen surface. This difference has previously been discussed elsewhere [27]. In contrast, the 0.6 wt.% Fe specimen has large β-intermetallic particles that can severely reduce the permeability of the mush by blocking the interdendritic flow paths [10,11,55], and thus, liquid feeding of the strained regions is much more difficult. Since β-intermetallics also act as stress concentrators, larger intermetallics weaken the mush [62] and therefore largely contribute to hot-tearing failure at very low true strains (Fig. 6b).

3.2.2. Post-failure observation

Longitudinal sections of the post-failure high-resolution (0.9 μm) tomographic images showing the fracture surfaces for both the 0.2 and the 0.6 wt.% Fe tensile specimens are

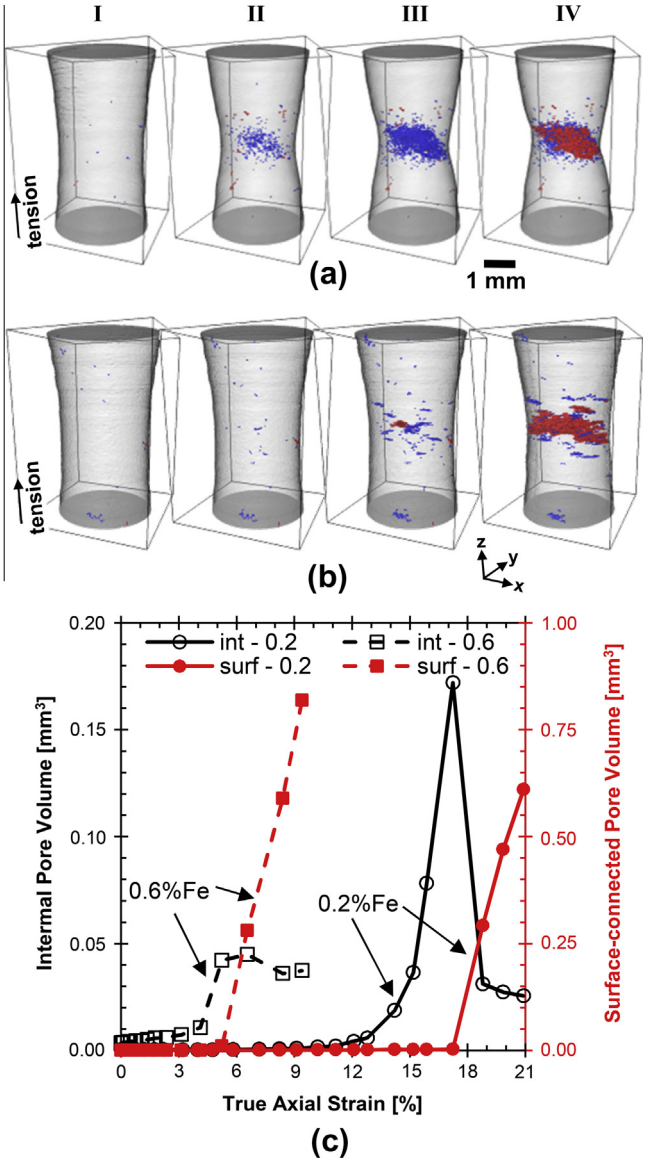

Fig. 6. 3-D rendering of hot tearing in Al–7.5Si–3.5Cu with (a) 0.2 wt.% Fe and (b) 0.6 wt.% Fe as well as the quantified evolution of: (c) the internal damage volume (int) and surface-connected damage volume (surf). I–IV represent true strains (%) of 0, 14, 17, 19 and 0, 4, 5, 7 for specimens with 0.2 and 0.6 wt.% Fe, respectively. Note that internal damage is coloured in blue and surface-connected damage coloured in red in (a) and (b). (For interpretation of the references to colour in this figure legend, the reader is referred to the web version of this article.)

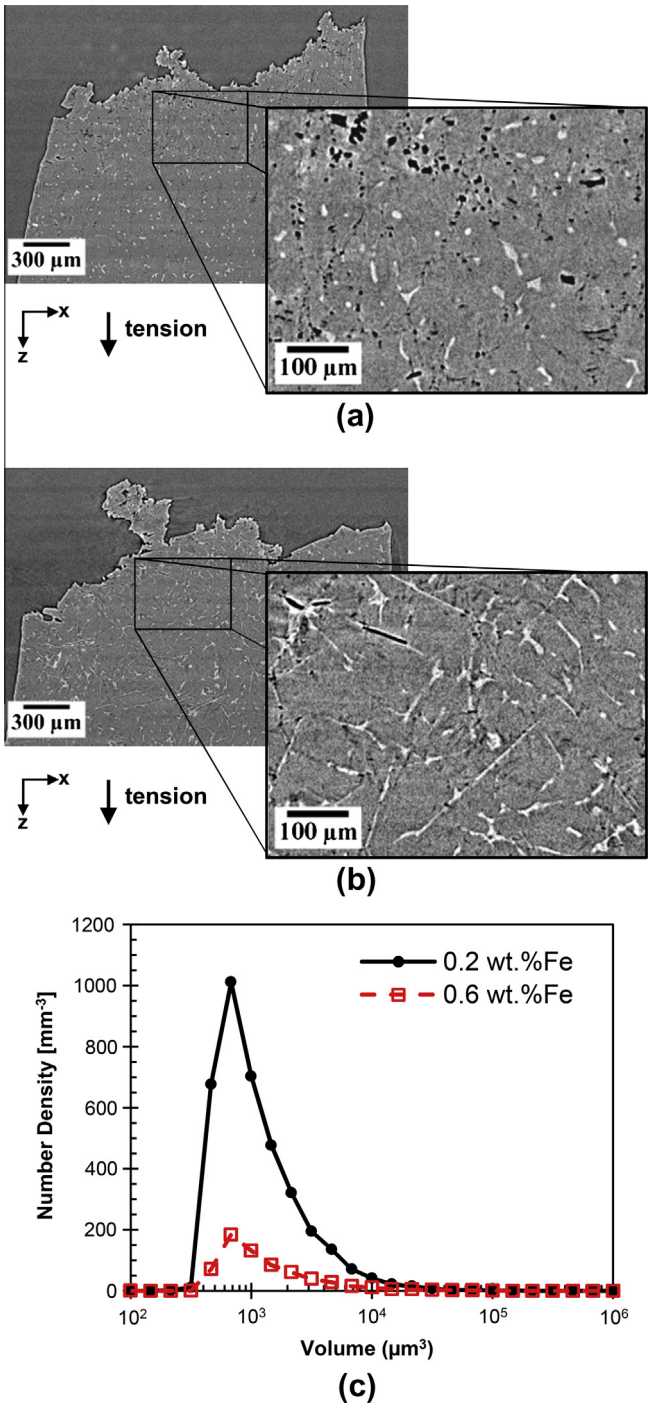

Fig. 7. (a and b) Longitudinal sections of post-failure microstructures in Al–7.5Si–3.5Cu with 0.2 and 0.6 wt.% Fe, respectively. (c) Quantified number density and volume of internal voids in both post-failure microstructures.

displayed in Fig. 7a and b, respectively. The damage voids appear dark, the aluminium grains appear grey and the β-intermetallics appear white. The magnified microstructure in Fig. 7a reveals a large number of internal voids near the fracture surface of the specimen with 0.2 wt.% Fe. Most of these internal voids appear round or elongated perpendicular to the loading direction. In contrast, the post-failure microstructure of the 0.6 wt.% Fe specimen in Fig. 7b exhibits significantly fewer internal voids near the fracture surface. There are a few voids that appear almost planar, and many of them are in contact with β-intermetallics. The number density distributions of post-failure internal voids for both specimens are given in Fig. 7c. Although the shape of the curves is similar, there is 5-fold increase in mode for the 0.2 wt.% Fe specimen. This clearly indicates that a different failure mechanism is operative.

By using two pores chosen at random near the fracture surfaces, the difference in internal void morphology in the

two specimens after hot-tearing failure is illustrated in Fig. 8. In the 0.2 wt.% Fe specimen, the void is clearly tortuous, branching and twisting along the complex interdendritic spaces (Fig. 8a). The void is coloured by local mean curvature to aid in visualizing its convexity and concavity. In contrast, the presence of large β-intermetallics, rendered in grey in the 0.6 wt.% Fe specimen (Fig. 8b), introduces an additional physical constraint and alters void morphology, creating a flatter and less branched void that is preferentially aligned along the planar surface of the β-intermetallic.

3.3. Discussion

The in situ observations of solidification and semi-solid deformation provide new insights into the role that β-intermetallics play in assisting the formation of casting defects. By comparing Figs. 8b with 4, it can be seen that the flat void morphology along the surface of β-intermetallics resulting from hot tearing is similar to the in situ observation of pore growth during solidification, where pores were seen to grow preferentially along β-intermetallics. Roy et al. [12] previously found that pores were always in contact with β-intermetallics in 2-D quenched Al–Si–Cu microstructures and implied that β-intermetallics are active nucleation sites for pores. These observations are not supported by the current work. First, there is no evidence of pore nucleation on β-intermetallics (as reported in prior quenched solidification [12]) in the tomographic images of in situ solidification. Second, if β-intermetallics were a potent pore nucleation site, there would have been a notable increase in pore density in the 0.6 wt.% Fe specimens when compared to the 0.2 wt.% Fe specimen, which was not observed. During isothermal semi-solid deformation, β-intermetallics do not appear as sites for void nucleation; instead, they enhance growth, potentially due to lower gas–intermetallic interfacial energy [13] or strain localization [63]. It is worth noting that the lower permeability caused by the presence of the large intermetallics also plays a significant role in the increase in damage at equivalent strain. This is shown in Fig. 6c where the 0.6 wt.% Fe specimen exhibits much more damage as compared to the 0.2 wt.% Fe specimen at the same amount of deformation. The resulting quasi-planar pore morphology may additionally impose strain localization at the tip of the pores combined with the stress concentration promoted by the β-intermetallics themselves. Phillion et al. [61] previously found that as-cast pores and newly formed voids acted as precursors to hot tearing. The influence of β-intermetallics on facilitating pore/void growth as well as altering pore/void morphology may also promote the initiation of hot tears.

Correlating the orientation of internal voids to loading direction is also of great interest. The orientation of each internal void in the post-failure microstructures was determined using PCA and compared to the tensile direction in order to quantify final void direction under uniaxial tension. A pole figure was obtained for each void, and schematics I–IV at the top of Fig. 9 illustrate the orientations of the voids. For example, a pole at the center of the plot corresponds to a void having a major axis (orientation) parallel to the tensile direction (Fig. 9-I), whereas a pole on the circumference of the plot corresponds to a void with a major axis perpendicular to the tensile direction (Fig. 9-IV). By integrating all pole figures, an orientation contour plot is obtained (Fig. 9a and b), where higher concentrations of orientations are shown in red and each calculated pole figure is shown as a white dot. In both specimens, the highest concentrations are found lying near the circumference of the image, indicating that internal voids in both specimens are preferentially oriented perpendicular to the loading direction. This is consistent with both Phillion et al. [61], who has shown through post-mortem tomographic imaging that crack propagation in semi-solids occurs in the direction perpendicular to loading to utilize the maximum strain energy for new crack surface creation, and also Sistaninia et al. [64–66], who performed combined

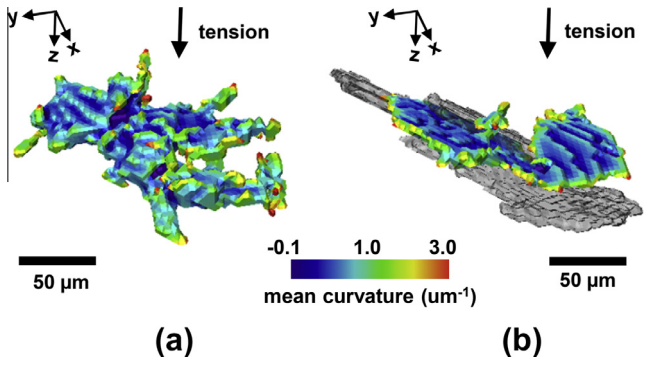

Fig. 8. (a and b) 3-D rendering of internal voids (coloured by local mean curvature) near the fracture surface of Al–7.5Si–3.5Cu with 0.2 and 0.6 wt.% Fe, respectively. Intermetallics in (b) are shown in grey. (For interpretation of the references to colour in this figure legend, the reader is referred to the web version of this article.)

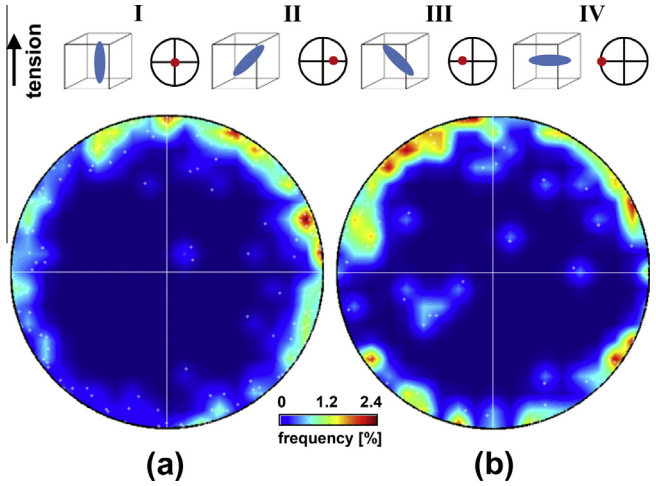

Fig. 9. Orientation contour plot of all internal voids in post-failure microstructures of Al–7.5Si–3.5Cu with (a) 0.2 wt.% Fe and (b) 0.6 wt.% Fe. Insets I–IV show a schematic orientation plot (each dot in circle) of an object with four different orientations.

discrete/finite-element simulations to demonstrate that strain development in high-fraction solid is concentrated only along a few preferential liquid paths perpendicular to the loading direction.

Finally, these in situ observations may help explain the industrially observed reduction in hot tearing that occurs through TiB_2 grain refinement and Sr modifications in Al–Si–Cu alloys [15,16]. These additions result in finer and shorter β-intermetallics [9,21], and in conjunction with the results presented here, it can be hypothesized that such changes in intermetallic size and shape would greatly reduce the impact of β-intermetallics on flow blockage and stress concentration, which in turn leads to a reduction in hot-tearing tendency. It is worth noting that the smaller grain size resulting from the addition of TiB_2 also contributes to reducing hot tearing by postponing the coherency solid fraction [67] and shrinking porosity albeit with a higher number density [22].

4. Conclusions

The influence of Fe-rich β-intermetallics on solidification defect formation has been quantitatively investigated using 4-D (three spatial dimensions evolving with time) synchrotron X-ray tomographic microscopy. Two experiments were conducted in this work: an in situ solidification study of porosity formation and an in situ isothermal semi-solid deformation experiment simulating hot tearing. The experiments were performed on a commercial A319 alloy (Al–7.5Si–3.5Cu, wt.%) with 0.2 and 0.6 wt.% Fe, providing complex commercial-like casting microstructures with β-intermetallic particles equivalent to primary and recycled aluminium alloy products.

From the in situ solidification experiment, the results indicate that the presence of a large fraction of β-intermetallics strongly blocks the interdendritic channels and induces porosity formation as a result of permeability reduction and hydrogen supersaturation in the local subdivided domain. No β-intermetallics are seen directly nucleating a pore during solidification; instead they appear to physically block and constrain pore growth and contribute to an increase in pore tortuosity. In addition, β-intermetallics are found to facilitate pore growth, which may be due to a low interfacial energy between the gas and the intermetallic plates.

The in situ semi-solid deformation experiments show that β-intermetallics increase hot-tearing susceptibility. The 0.6 wt.% Fe specimen sustained a relatively small amount of strain ($\varepsilon \sim 7\%$) prior to failure, and the failure event was brittle-like. In comparison, the 0.2 wt.% Fe specimen sustained triple the true strain upon failure, and the failure event was more ductile. High-resolution images of the β-intermetallic-rich post-failure microstructures also show that the internal pores near the fracture surface of the 0.6 wt.% Fe specimen were flatter, less branched and preferentially aligned to existing β-intermetallics in comparison to the 0.2 wt.% Fe sample, which exhibited highly tortuous and branched pores. Such a change in the pore shape could concentrate strain and weaken the mush. These advancements in observing and quantifying intermetallics and defect formation highlight the very complex effect of secondary phase formation on the rheology and mechanical behaviour of semi-solid microstructures.

Acknowledgements

The authors would like to acknowledge the provision of beamtime and help from the beamline staff, particularly G. Mikuljan at the TOMCAT beamline of the SLS and the scientists at the I12 beamline, Diamond Light Source (Experiment No. EE7604). Thanks also to P. Rockett, R.W. Hamilton and J. Wang for help with the design of the in situ rig and material preparation. The authors also would like to thanks EPSRC (EP/I02249X/1), M-ORS, a Thai Government Scholarship, Ford Motor Company and the Research Complex at Harwell for financial, materials and facilities support. J.L.F. would also like to acknowledge CCMX for funding.

Appendix A. Supplementary material

Supplementary data associated with this article can be found, in the online version, at http://dx.doi.org/10.1016/j.actamat.2014.01.007.

References

[1] Lee PD, Lindley TC, Cheong CWJ, Davis GR, Elliott J. In: Proceedings of COM. Vancouver, BC; 2003. p. 457.
[2] Yi JZ, Gao YX, Lee PD, Lindley TC. Mater Sci Eng A 2004;386:396.
[3] Crepeau P. AFS Trans 1995;103:361.
[4] Li Z, Samuel AM, Samuel FH, Ravindran C, Valtierra S, Doty HW. Mater Sci Eng A 2004;367:96.
[5] Li Z, Samuel AM, Samuel FH, Ravindran C, Doty HW, Valtierra S. Mater Sci Eng A 2004;367:111.
[6] Ma Z, Samuel AM, Samuel FH, Doty HW, Valtierra S. Mater Sci Eng A 2008;490:36.
[7] Samuel AM, Pennors A, Villeneuve C, Samuel FH, Doty HW, Valtierra S. Int J Cast Met Res 2000;13:231.
[8] Taylor J, Schaffer G, StJohn D. Metall Mater Trans A 1999;30:1643.
[9] Lu L, Dahle A. Metall Mater Trans A 2005;36:819.
[10] Dinnis CM, Taylor JA, Dahle AK. Mater Sci Eng A 2006;425:286.
[11] Dash M, Makhlouf M. J Light Met 2001;1:251.
[12] Roy N, Samuel A, Samuel F. Metall Mater Trans A 1996;27:415.
[13] Wang J, Li M, Allison J, Lee PD. J Appl Phys 2010;107:061804.
[14] Dinnis C, Taylor J, Dahle A. Metall Mater Trans A 2006;37:3283.
[15] Paray F, Kulunk B, Gruzleski JE. Int J Cast Met Res 2000;13:147.
[16] D'Elia F, Ravindran C. T Indian I Metals 2009;62:315.
[17] Guven YF, Hunt JD. Cast Metals 1988;1:104.
[18] Farup I, Drezet JM, Rappaz M. Acta Mater 2001;49:1261.
[19] Rappaz M, Drezet JM, Gremaud M. Metall Mater Trans A 1999;30A:449.
[20] Eskin DG, Suyitno, Katgerman L. Prog Mater Sci 2004;49:629.
[21] Khalifa W, Samuel F, Gm Nserc U, Gruzleski J, Doty H, Valtierra S. Metall Mater Trans A 2005;36:1017.
[22] Lee PD, Hunt JD. Acta Mater 1997;45:4155.
[23] Lee PD, Wang J, Atwood RC. JOM-e 2006; online only.
[24] Lee PD, Chirazi A, See D. J Light Met 2001;1:15.
[25] Arnberg L, Mathiesen R. JOM 2007;59:20.

[26] Phillion AB, Hamilton RW, Fuloria D, Leung ACL, Rockett P, Connolley T, et al. Acta Mater 2011;59:1436.
[27] Puncreobutr C, Lee P, Hamilton R, Cai B, Connolley T. Metall Mater Trans A 2013;44:5389.
[28] Terzi S, Salvo L, Suéry M, Limodin N, Adrien J, Maire E, et al. Scripta Mater 2009;61:449.
[29] Suéry M, Terzi S, Mireux B, Salvo L, Adrien J, Maire E. JOM 2012;64:83.
[30] Terzi S, Salvo L, Suéry M, Adrien J, Maire E, Boller E. Mater Sci Forum 2009;618–619:275.
[31] Terzi S, Taylor JA, Cho YH, Salvo L, Suéry M, Boller E, et al. Acta Mater 2010;58:5370.
[32] Tolnai D, Townsend P, Requena G, Salvo L, Lendvai J, Degischer HP. Acta Mater 2012;60:2568.
[33] Limodin N, Salvo L, Boller E, Suéry M, Felberbaum M, Gaillièque S, et al. Acta Mater 2009;57:2300.
[34] Terzi S, Salvo L, Suery M, Dahle AK, Boller E. Acta Mater 2010;58:20.
[35] Limodin N, Salvo L, Suéry M, DiMichiel M. Acta Mater 2007;55:3177.
[36] Maire E, Withers PJ. Int Mater Rev 2014;59:1.
[37] Yi J, Gao Y, Lee P, Flower H, Lindley T. Metall Mater Trans A 2003;34:1879.
[38] Du Y, Schuster JC, Liu Z-K, Hu R, Nash P, Sun W, et al. Intermetallics 2008;16:554.
[39] Fife JL, Rappaz M, Pistone M, Celcer T, Mikuljan G, Stampanoni M. J Synchrot Radiat 2012;19:352.
[40] Stampanoni M, Groso A, Isenegger A, Mikuljan G, Chen Q, Bertrand A, et al. In: Proceedings of developments in X-ray tomography V; 2006. p. 63180M.
[41] Mokso R, Marone F, Stampanoni M. AIP Conf Proc 2010;1234:87.
[42] Puncreobutr C. 2013. In situ synchrotron characterisation of Fe-rich intermetallic formation during the solidification of Al-Si-Cu-Fe alloys. PhD Thesis. Imperial College London: UK.
[43] Marone F, Munch B, Stampanoni M. In: Proceedings of developments in X-ray tomography VII; 2010. p. 780410.
[44] Marone F, Stampanoni M. J Synchrot Radiat 2012;19:1029.
[45] Titarenko S, Titarenko V, Kyrieleis A, Withers PJ, De Carlo F. J Synchrot Radiat 2011;18:427.
[46] Titarenko V, Bradley R, Martin C, Withers PJ, Titarenko S. In: Proceedings of developments in X-ray tomography VII; 2010. p. 78040Z.
[47] Kyrieleis A, Titarenko V, Ibison M, Connolley T, Withers PJ. J Microsc 2011;241:69.
[48] Münch B, Trtik P, Marone F, Stampanoni M. Opt Exp 2009;17:8567.
[49] Studholme C. Patt Recogn 1999;32:71.
[50] Weickert J, Haar B, Viergever R. IEEE T Image Process 1998;7:398.
[51] Adams R, Bischof L. IEEE T Patt Anal 1994;16:641.
[52] Puncreobutr C, Lee P, Hamilton R, Phillion A. JOM 2012;64:89.
[53] Yue S, Lee PD, Poologasundarampillai G, Jones JR. Acta Biomater 2011;7:2637.
[54] Wang J, Lee PD, Hamilton RW, Li M, Allison J. Scripta Mater 2009;60:516.
[55] Puncreobutr C, Phillion AB, Fife JL, Lee PD. Acta Mater 2014;64:316.
[56] Felberbaum M, Rappaz M. Acta Mater 2011;59:6849.
[57] Otte M, McDonald S, Taylor J, StJohn D, Schneider W. AFS Trans 1999;107:471.
[58] Landron C, Maire E, Bouaziz O, Adrien J, Lecarme L, Bareggi A. Acta Mater 2011;59:7564.
[59] Kaye M, Puncreobutr C, Lee PD, Balint DS, Connolley T, Farrugia D, et al. Acta Mater 2013;61:7616.
[60] Puncreobutr C, Lee PD, Kaye M, Balint D, Farrugia D, Connolley T, et al. IOP Conf Ser: Mater Sci Eng 2012;33:012038.
[61] Phillion AB, Lee PD, Maire E, Cockcroft SL. Metall Mater Trans A 2008;39:2459.
[62] Sweet L, Easton M, Taylor J, Grandfield J, Davidson C, Lu L, et al. Metall Mater Trans A 2012;1.
[63] Gao YX, Yi JZ, Lee PD, Lindley TC. Acta Mater 2004;52:5435.
[64] Sistaninia M, Phillion AB, Drezet JM, Rappaz M. Metall Mater Trans A 2011;42:239.
[65] Sistaninia M, Phillion AB, Drezet JM, Rappaz M. Acta Mater 2012;60:3902.
[66] Sistaninia M, Terzi S, Phillion AB, Drezet JM, Rappaz M. Acta Mater 2013;61:3831.
[67] Veldman NM, Dahle A, StJohn D, Arnberg L. Metall Mater Trans A 2001;32:147.